11-1-2023

Effect of thermal capacitance on microchannel heat sink response to pressure drop oscillations

M. D. Clark

M. E. Rahman

Justin A. Weibel
jaweibel@purdue.edu

S. V. Garimella

Clark, M. D.; Rahman, M. E.; Weibel, Justin A.; and Garimella, S. V., "Effect of thermal capacitance on microchannel heat sink response to pressure drop oscillations" (2023). *CTRC Research Publications.* Paper 408.
http://dx.doi.org/https://doi.org/10.1016/j.ijheatmasstransfer.2023.124369

Effect of Thermal Capacitance on Microchannel Heat Sink Response to Pressure Drop Oscillations

Matthew D. Clark, Md Emadur Rahman, Justin A. Weibel[1], Suresh V. Garimella[2]
Cooling Technologies Research Center, School of Mechanical Engineering
Purdue University, 585 Purdue Mall, West Lafayette, IN 47907 USA

Abstract

The efficient heat transfer resulting from flow boiling in microchannel heat sinks can help dissipate high heat fluxes from high-density electronic devices across a small temperature difference. However, practical implementation challenges unique to two-phase flow boiling, as compared to single-phase liquid cooling, have prevented its widespread adoption. A primary challenge is the occurrence of dynamic two-phase flow instabilities, such as pressure drop oscillations (PDO), that have the potential to degrade heat transfer performance or trigger premature critical heat flux (CHF) under some conditions. Under other conditions, PDOs are observed to have little to no impact on performance. One factor proposed by modeling studies to be responsible for this discrepancy in observations of the effect of dynamic instabilities on performance is the thermal capacitance of the heat sink, though this has not been confirmed by experiments. In this study, the effect of thermal capacitance on the transient thermal response of a heat sink experiencing PDOs is examined through use of a dynamic two-phase flow model and experiments. Flow boiling experiments are performed with a controlled compressible volume upstream of parallel-microchannel heat sinks having either a large or a small thermal capacitance. In accordance with the behavior predicted by our model, when thermal capacitance is reduced, the pressure drop oscillation frequency is found to decrease and temperature swings in the heat sink become more severe. Additionally, the experimentally measured CHF limit is diminished in the heat sink at smaller thermal capacitance. These results reveal thermal capacitance as a critical parameter that determines how much dynamic instabilities degrade flow boiling performance in a microchannel heat sink.

Keywords

Flow boiling; instabilities; compressibility; microchannels; two-phase heat transfer; electronics cooling

[1] Corresponding author E-mail address: jaweibel@purdue.edu
[2] Suresh Garimella is currently with The University of Vermont, Burlington, VT 05405 USA.

Nomenclature

A_c	Channel cross-sectional area [m^2]
A_f	Channel footprint area [m^2]
A_p	Pipe cross-sectional area [m^2]
A_s	Heat transfer surface area [m^2]
C_p	Specific heat [J/kgK]
d_{eff}	Effective thermal depth [m]
f	Frequency [Hz]
G	Nominal mass flux in experiments [kg/m^{2}s]
G_{buf}	Mass flux to buffer tank [kg/m^{2}s]
G_{in}	Mass flux to channel [kg/m^{2}s]
h	Heat transfer coefficient [W/m^{2}K]
h_c	Channel height [m]
I	Current [A]
L_c	Channel length [m]
m	Heat sink mass [kg]
m_{eff}	Effective thermal mass [kg]
N	Number of channels [-]
$\hat{P}$	$P_{inlet} - P_{inlet,mean}$ [Pa]
P_{amb}	Ambient pressure [Pa]
P_{buf}	Buffer tank pressure [Pa]
P_{elec}	Electrical power [W]
P_i	Initial pressure of compressible volume [Pa]
P_{inlet}	Inlet manifold pressure [Pa]
P_{outlet}	Outlet manifold pressure [Pa]
P_{system}	System pressure [Pa]
ΔP_c	Channel pressure drop [Pa]
ΔP_i	Inlet header pressure drop [Pa]
ΔP_o	Outlet header pressure drop [Pa]
Q_{loss}	Heat loss [W]
q^*	Instantaneous heat absorbed by fluid ($hA_s(T_s - T_f)$) [W]
$q"$	Wetted-area heat flux [W/cm^2]
q'	Heat input per channel length [W/m]

t	Time [s]
$T_{\#}$	Heat sink thermocouples (T_1, T_2, T_3) [°C]
T_f	Mean fluid temperature [°C]
T_i	Initial temperature [°C]
T_{in}	Fluid temperature at channel inlet [°C]
T_{mean}	Mean temperature [°C]
T_{ref}	Fluid reference temperature [°C]
T_s	Heat sink surface temperature [°C]
T_{sub}	Inlet subcooling ($T_{sat} - T_{in}$) [°C]
V	Voltage [V]
V_i	Initial compressible volume [ml]
w_c	Channel width [m]
x	Vapor quality $\left(\frac{h-h_f}{h_g-h_f}\right)$

Greek symbols

α	Thermal diffusivity [m^2/s]
$\delta_{p,\omega}$	Penetration depth for periodic temperature ($4\sqrt{\alpha/(2\pi f)}$) [m]
δ_p	Penetration depth for step change in temperature ($2\sqrt{\alpha t}$) [m]
λ	Period ($1/f$) [s]
ρ_f	Fluid density [kg/m^3]
ρ_w	Heat sink density (copper) [kg/m^3]

1 Introduction

Applications such as radar systems, high-performance computing, and power electronics will soon necessitate cooling technologies with capabilities that exceed current state-of-the-art single-phase cold plates or air-cooled heat sinks ([1]–[3]). The efficient heat transfer mechanisms associated with phase change during microchannel flow boiling can provide the means to dissipate high-density heat loads from next-generation electronic devices, reaching in excess of 1000 W/cm^2 in prototype demonstrations ([4]–[7]). Flow boiling also provides the advantages of increased temperature uniformity and decreased pumping power requirements due to the high latent heat and isothermal nature of phase-change. However, there are unique challenges associated with implementing flow boiling as a cooling technology, including the difficulty in predicting heat transfer and pressure drop, inherent critical heat flux (CHF) limitations, and the presence of flow boiling instabilities that can degrade these performance measures. In microscale systems where vapor confinement and bubble clogging is more likely, flow boiling instabilities are of particular concern [8].

Two broad categories of flow boiling instabilities are static and dynamic instabilities ([9], [10]). Static instabilities, such as the Ledinegg instability, are characterized by a flow which transitions from one operation condition to a different one. These are also referred to as flow excursions and have been studied extensively in microchannel heat sinks ([11]–[14]). Dynamic instabilities, on the other hand, are characterized by interaction between a two-phase mixture in a heated channel and a source of compressibility beyond the channel ([9], [15]). In microchannel heat sinks, dynamic instabilities of concern include parallel channel instabilities, density wave oscillations, and pressure drop oscillations (PDO). It is possible for these instabilities to degrade heat sink performance, besides causing wall temperature oscillations, vibration, increased surface temperatures, and early onset of critical heat flux ([16]–[18]). Much of the attention given to dynamic instabilities in microchannel heat sinks focuses on suppression techniques, often at the expense of increased pumping power or fabrication complexity ([8], [19]–[22]). However, our recent studies have shown that pressure drop oscillations and parallel channel instabilities have little impact on time-averaged surface temperatures and CHF under some conditions ([23], [24]). The occurrence, severity, and impact of instabilities can depend on many factors, such as heat sink geometry, fluid properties, and operating conditions ([13], [25], [26]). It is necessary to better understand when instabilities are of concern in microchannel heat sinks and when their effect may be neglected compared to the cost of suppression. Previous studies that model the PDO dynamics have suggested that thermal capacitance (mC_p) can significantly alter the severity of oscillations ([27]–[31]), but lack any experimental validation or demonstration of this effect. As background, we first elaborate on the underlying PDO instability mechanism below.

Unique to flow boiling, the pressure drop across a channel with a subcooled liquid inlet can increase with decreasing mass flux for a constant heat input. This is due to an increase in vapor generation at lower mass flux that results in vapor bubble growth, acceleration, and confinement. A typical N-shaped channel pressure demand curve for a constant heat input is shown in Figure 1(a). Three regions of the curve are distinguished by the outlet vapor quality. The low mass flux region (I) is characterized by high outlet vapor quality where the incoming fluid is quickly vaporized and the channel is primarily in the vapor phase along its length. The negative-slope region (II) at intermediate mass fluxes is characterized by a two-phase liquid-vapor mixture at the outlet. The third region (III) at high mass flux is characterized by subcooled liquid at the outlet, as the given heat input is insufficient to raise the inlet subcooled liquid to the saturation temperature before it reaches the channel outlet. The vertical, red line marked G_0 in Figure 1(a) denotes a constant mass flux supply curve, which would result in stable operation at the operating point (red dot) intersecting the demand curve if only considering the pump and channel alone. However, if a compressible volume is present upstream of the channel, this operating point becomes unstable, resulting in pressure drop oscillations ([9], [26], [29], [32]). During a PDO cycle, the instantaneous channel mass flux and pressure drop follow a path marked by the arrows and the dashed green line (limit cycle) bounded by the channel demand curve as shown in Figure 1(a); the associated transient channel mass flux is shown in Figure 1(b). The primary concern from PDOs that impacts heat sink thermal performance is associated with the low mass flux region of the cycle. The mass flux suddenly drops from point A to B, and increased vapor generation within the channel occurs between B and C while the compressible volume upstream of the channel pressurizes as it collects a portion of the mass flux from the constant mass flux supply G_o. During the duration of this event, which occurs periodically, the fluid is mostly in the vapor phase within the channel, reducing the rate at which heat can be extracted from the channel surface and increasing the surface temperatures. In the limit cycle shown here, the upstream pressure will recover, and the channel mass flux will increase to point D, reducing fluid temperatures and again increasing the rate at which heat can be extracted. However, under some conditions, it is possible that the upstream pressure will not recover in time to rewet the channel before dryout occurs, triggering premature CHF. A large thermal capacitance acts to slow the temperature rise with respect to the limit cycle time and can thereby potentially mitigate the transient surface temperature oscillations.

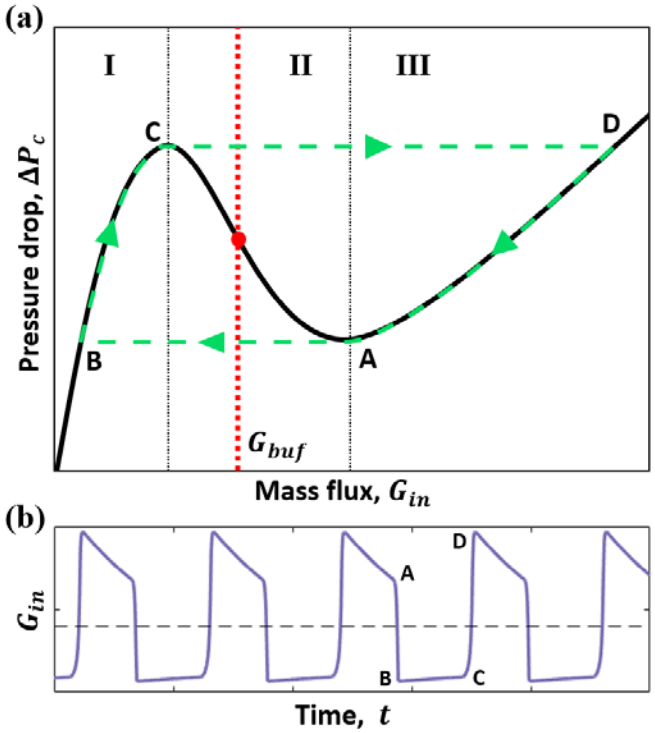

Figure 1. (a) Characteristic N-shaped channel demand curve for flow in a channel with subcooled liquid inlet and constant heat input (solid black line) divided into regions I, II, and III. In the presence of upstream compressibility, the intersecting operating point (red dot) of the channel demand curve and constant mass flux supply curve (red dashed line) is unstable, and the channel inlet mass flux follows a limit cycle (dashed green lines with arrows) characteristic of pressure drop oscillations. (b) Representation of the transient channel mass flux during pressure drop oscillations.

In this work, the effect of thermal capacitance, or mass, of a microchannel heat sink on the transient response to pressure drop oscillations is studied using a dynamic model and through experiments. To first confirm that the dynamic model, which includes coupling of the two-phase flow dynamics with the transient heat sink thermal response, reasonably predicts the trends in PDO frequency and peak-to-peak temperature oscillation amplitude, the model predictions are compared against experimental data. The model is then exercised to predict oscillation dynamics of selected large- versus small-mass heat sinks in which we experimentally demonstrate the critical role of heat sink thermal capacitance. Experiments are performed in a heat sink with N = 12 channels of width w_c = 0.75 mm at a mass flux of G = 400 kg/m^{2}s and heat fluxes ranging from 16 – 28 W/cm^2 with a controlled degree of upstream compressibility. The effect of thermal capacitance on heat sink thermal response to the pressure

drop oscillation instability is assessed through analysis of the time-averaged heat transfer data, transient temperature and pressure data, and flow visualizations.

2 Experimental Methods

This section describes details of the experimental test section, flow loop, and procedures custom-designed to accommodate upstream compressibility control. An example data set is also presented which shows the occurrence of pressure drop oscillation instability.

2.1 Test Section and Flow Loop

The test section housing a microchannel heat sink, originally developed in Ref. [23] and modified for the current work, is shown in cross-section in Figure 2(a). Twelve w_c = 0.75 mm square-cross-section channels are machined into a copper block with a footprint area of 2 cm × 2 cm. The actual as-fabricated channel dimensions measured under a microscope (Olympus BX53M) are w_c = 0.85 mm × h_c = 0.83 mm. Three T-type thermocouples are inserted into holes in the side of the heat sink, positioned streamwise along the centerline 2.5 mm below the top surface as shown in the detailed view of Figure 2(b). Heat is supplied by a small-form-factor ceramic heater with overall dimensions of 12 mm × 12 mm × 2.5 mm (Watlow CER-1-01-00540) equipped with an embedded K-type thermocouple for monitoring the device temperature. A thermal interface material (Laird Tflex 700) is placed between the ceramic heater and the bottom face of the heat sink. Power dissipated by the heater is calculated as $P_{elec} = IV$, where the supply current I is measured using a shunt resistor and the voltage V is measured at the power supply. The heater is held in place by the compression assembly shown in Figure 2(a). A ceramic spacer is used to fill the space below the heat sink that originally accommodated a larger copper heater block in Ref. [23]. Heat losses from the ceramic heater are assumed to be negligible.

The assembly surrounding the heat sink and heater are machined from polyetheretherketone (PEEK). Fluid is routed through plenums and headers machined into the PEEK housing. Ports for measurement of pressure and temperature are located in the inlet and outlet plenums as identified in Figure 2(a). To seal the top open surfaces of the PEEK housing and the heat sink channels, a silicone gasket is compressed between the assembly and a polycarbonate lid, which also allows for visualization of flow in the heat sink. To prevent the silicone gasket from squashing into the channels and blocking flow, a thin film of rigid polyethylene terephthalate (PET) is placed over the top surface area of the heat sink underneath the silicone gasket. Mating surfaces between the PEEK housing and the copper heat sink are sealed using a silicone adhesive (Momentive RTV118).

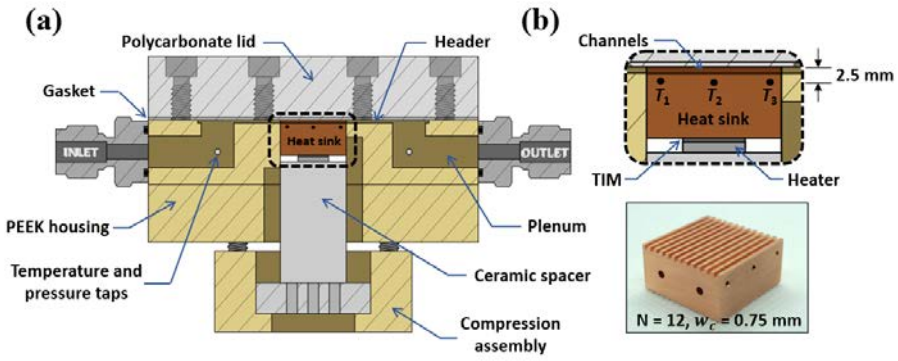

Figure 2. (a) Cross section of test section assembly with key components identified and (b) heat sink detail view and photograph.

The flow loop shown schematically in Figure 3 is charged with the dielectric fluid HFE-7100 [33], which is degassed prior to and during experiments by maintaining saturated conditions within the custom-built reservoir equipped with immersion heaters and Graham condensers connected to an external chilled water supply. The supply mass flow rate is precisely controlled by setting the motor speed of the positive displacement gear pump (Micropump GB-P23) and regulating a portion of the flow that bypasses back into the reservoir. Contaminants are removed from the fluid by a combination of particulate and activated carbon filters upstream of the Coriolis mass flowmeter (Micromotion CMF010M). The desired inlet subcooling to the test section is controlled by an electrical preheater located downstream of the flowmeter.

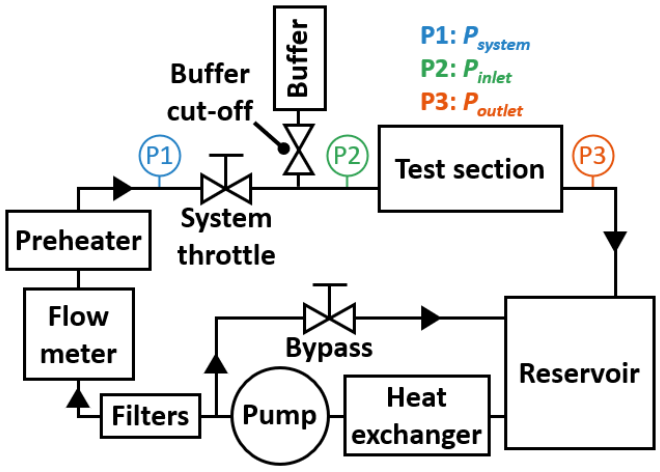

Figure 3. Diagram of the experimental flow loop.

To control the degree of upstream compressibility to which the test section is exposed, the flow is throttled after the preheater using the needle valve labeled “system throttle” in Figure 3. Throughout all experiments, the pressure upstream of this valve is maintained at least an order of magnitude above the nominal pressure drop across the test section. This effectively isolates all components downstream of the system throttle from interacting dynamically with the upstream components. Directly downstream of the system throttle valve, a buffer volume consisting of a custom-fabricated glass tube with threaded connections on either end is plumbed into a T-junction. The buffer volume is mounted vertically, perpendicular to the flow from the system throttle valve, and is free to interact with the test section. To introduce a set volume of compressibility, the top cap of the buffer volume is removed, and the ball valve labeled “buffer cut-off” in Figure 3 situated between the buffer volume and the main flow line is opened until the liquid level within the buffer volume reaches a predetermined height as measured by the graduations. The ball valve is then closed, and the cap replaced, trapping a consistent, measurable volume of air at atmospheric pressure within the buffer volume. The ball valve is then opened again, exposing the flow to the compressible volume. A float placed inside the buffer volume minimizes the liquid-air interfacial area and prevents evaporation of the working fluid or absorption of air into the working fluid during the experiment. Throughout all tests, the initial volume of air within the buffer volume is set to 35 ml.

2.2 Experimental Procedure

After degassing for a minimum of 2 hr by vigorously boiling the liquid in the reservoir while allowing non-condensable gases to escape through the Graham condensers, each experiment begins by setting the inlet subcooling to T_{sub} = 20 °C and mass flux to G = 400 kg/m^{2}s while maintaining a system pressure of P_{system} = 90 – 100 kPa above the test section outlet pressure. Inlet subcooling is calculated as the difference between the saturation temperature of the working fluid at atmospheric pressure as maintained at the test section outlet and the liquid temperature measured at the test section inlet plenum.

Power supplied to the heater is incremented in small steps across a range of heat fluxes (q'' = 16 – 28 W/cm^2). This range is chosen because it was identified in our previous work as where pressure drop oscillations will occur using this heat sink under the same boundary conditions [24]. At each power increment, the system is allowed to reach a steady state before data are recorded (National Instruments cRIO-9024). Data are recorded in two steps. First, to capture transient pressure fluctuations associated with PDOs, pressure transducers are sampled over 10 s at a high frequency of 25 kHz and averaged every 10 data points to reduce noise. A high-speed camera (Vision Research, Phantom v1212) is simultaneously triggered to synchronize these pressure signals with flow visualization. Second, all other sensors are sampled over 2 min at a lower frequency of 14 Hz for analysis of transient thermal response and time-averaged performance. Channel wetted-area heat flux is calculated using the electrical power supplied to the heater block ($q'' = P_{elec}/A_s$), where the heat transfer area A_s is the total area of the three copper sides of each channel. Uncertainty in key sensor measurements and extrapolated values are listed in Table 1.

Table 1. Summary of measurement uncertainty.

Measurement	Uncertainty
Calibrated T-type thermocouples	±0.3 °C
Pressure transducers	±2.13 kPa
Wetted-area heat flux	±0.02 W/cm^2 (lowest fluxes) to ±0.2 W/cm^2 (highest fluxes)
Extrapolated surface temperature	±0.4 °C

2.3 Example Post-Processed Transient Measurement Data

A representative experimental observation of a PDO cycle as it occurs in practice is illustrated here. Figure 4(a-c) shows a series of flow visualization snapshots in the w_c = 0.75 mm heat sink with a copper block height of 10 mm at a heat flux of q'' = 24 W/cm^2 during a PDO cycle. Underneath the

snapshots, Figure 4(d) plots the inlet pressure signal as $\hat{P}_{inlet} = P_{inlet} - P_{inlet,mean}$ and the location of each snapshot in time is marked by a red dashed line. The low frequency oscillation in Figure 4(d), highlighted by the rolling average of $\hat{P}_{inlet}$ plotted as a dashed black line, is a result of the PDO instability and the focus of this discussion, while high frequency noise between 0 – 1.5 s and 2.5 – 4.5 s is caused by parallel-channel interactions. In the first snapshot (Figure 4(a)), the instantaneous mass flux is high, and the fluid entering the microchannels remains as subcooled liquid over a portion of the channel length before boiling begins (marked as a dashed blue line) and the remaining length of the channels contains two-phase flow. This corresponds to the region between points D and A in Figure 1. In the second snapshot (Figure 4(b)), the mass flux is low, and the channels are filled with vapor, which is also expanding in the upstream direction into the inlet header covering all channel inlets, corresponding to point B in Figure 1. Vapor backflow into the inlet header results in the higher frequency and amplitude fluctuations between 1.5 – 2.5 s in Figure 4(d). In the final snapshot (Figure 4(c)), the mass flux is recovering back to the higher state as in the region between points B and C in Figure 1, and there is no longer vapor backflow due to pressure drop oscillations. However, backflow does still occur in some channels due to parallel-channel interactions.

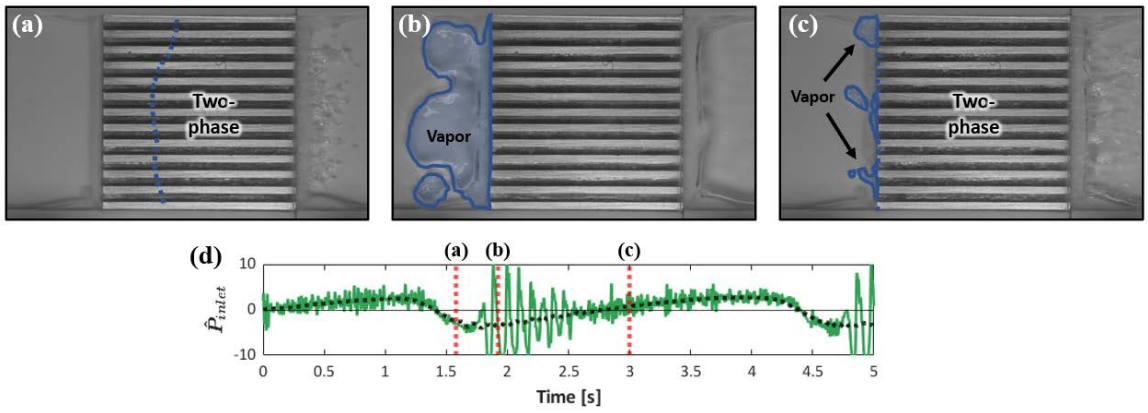

Figure 4. Snapshots (a-c) of flow in a heat sink with twelve w_c = 0.75 mm channels at a mass flux of G = 400 kg/m^{2}s and heat flux of q'' = 24 W/cm^2 experiencing pressure drop oscillation (PDO) instability. Boundaries between liquid and two-phase regions are marked by dashed blue lines and vapor bubbles in the inlet header are bounded by solid blue lines. Below the snapshots, $\hat{P}_{inlet} = P_{inlet} - P_{inlet,mean}$ is plotted over 5 s and the instant of each snapshot frame is noted by a dashed red line. The dashed black line is a rolling average of $\hat{P}_{inlet}$.

The temperature signal of the center thermocouple T_2 corresponding to the same conditions is plotted in Figure 5 over 60 s. The peak-to-peak amplitude of the temperature oscillation is approximately 2.5 °C and the frequency is 0.36 Hz. The heat sink experiences a rise in temperature during the low-mass-flux region of the PDO cycle due to the vapor backflow and rise in temperature of the fluid that stagnates in the heat sink. The minimum heat sink temperatures occur during the brief high-mass-flux region of the PDO cycle when fluid temperatures are reduced due to the inrushing subcooled liquid.

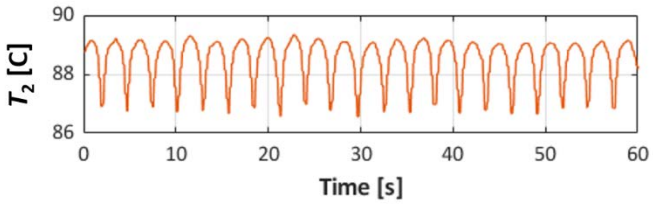

Figure 5. Temperature oscillations of the heat sink experiencing pressure drop oscillation instability at a mass flux of G = 400 kg/m^{2}s and heat flux of q'' = 24 W/cm^2.

3 Dynamic Model

In this section, a dynamic two-phase model is first described, and an example prediction of pressure drop oscillations is presented. Model predictions are then compared against results from a previous study [24].

3.1 Model Description

Figure 6 schematically represents a two-phase system where pressure drop oscillations could occur, comprising a heat sink and an upstream compressible volume. The system is supplied with a constant mass flux G_{buf} at the inlet to a buffer tank containing a trapped volume of compressible air at pressure P_{buf}. For simplicity, the heat sink is considered to have a lumped thermal capacitance mC_p at a uniform temperature T_s. Pressure losses due to friction, contraction, and expansion within the inlet and outlet headers are ΔP_i and ΔP_o, respectively, and the two-phase pressure drop within the channel is ΔP_c. A uniform, constant heat input per unit length q' is applied to the heat sink, though the instantaneous heat absorbed by the fluid can fluctuate during pressure drop oscillations, as governed by the convection heat transfer coefficient and temperature difference between the fluid and heat sink. The HFE-7100 fluid properties are evaluated at saturation conditions at the atmospheric outlet conditions P_{amb}.

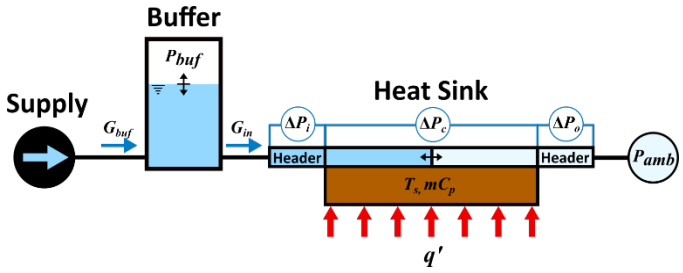

Figure 6. Schematic diagram of a two-phase system for analysis of pressure drop oscillations including a constant mass flux supply, buffer tank with compressible volume, and heat sink.

The three transient governing equations, originally derived in [26] and [31], are used to model the system response to pressure drop oscillations under the following assumptions:

1. The air within the buffer is at a constant temperature.
2. The supply mass flux is constant as representative of a constant volumetric gear pump used in experiments.
3. The instantaneous mass flux through the channel is uniform.

The first governing equation describes the continuity of mass in the buffer tank assuming an ideal gas and is written as

$$\frac{dP_{buf}}{dt} = \frac{P_{buf}^2\left(G_{buf}A_p - G_{in}A_c\right)}{\rho_f P_i V_i} \tag{1}$$

where A_p is the flow cross-sectional area of the tubing between the supply and the heat sink, A_c is the flow cross-sectional area in the heat sink, V_i is the initial compressible volume, and P_i is the initial pressure of the compressible volume.

The second governing equation is derived by integration of the one-dimensional momentum equation as

$$\frac{dG_{in}}{dt} = \frac{1}{L_c}\left(P_{buf} - P_{atm} - \Delta P_i - \Delta P_c - \Delta P_o\right) \tag{2}$$

where L_c is the channel length and P_{atm} is atmospheric pressure as maintained at the test section outlet in the experiments. The header pressure losses ΔP_i and ΔP_o are calculated using correlations developed for parallel channel heat sinks ([34], [35]) and calibrated to the experimental facility. Details for these calculations can be found in the Appendix. The channel pressure drop ΔP_c consists of acceleration,

friction, and gravitational pressure losses and is calculated using a one-dimensional separated-flow method as described in Ref. [26].

The third and final governing equation describes the transient thermal transport between the lumped thermal mass and the fluid as

$$\frac{dT_s}{dt} = \frac{1}{mC_p}\left(q'L_c - hA_s(T_s - T_f)\right) \tag{3}$$

where T_w is the uniform heat sink temperature, h is the heat transfer coefficient (assumed to be constant), A_s is the heat transfer surface area, and T_f is the fluid reference temperature. The set of ordinary differential equations (1)-(3) are solved numerically using the MATLAB [36] variable-step, variable order ODE15s solver.

3.2 Example Pressure Drop Oscillation Prediction

To demonstrate the prediction capabilities, the model is exercised using input conditions based on the experimental data set presented in Section 2.3. The nominal mass flux is G_{buf} = 400 kg/m^{2}s, heat input is q'' = 24 W/cm^2 (q' = 627 W/m), and inlet temperature is T_{in} = 41 °C. The heat transfer coefficient is specified based on experimental data (h = 7600 W/m^{2}K) and the per-channel thermal capacitance is mC_p = 1.1 J/K. The initial compressible volume is V_i = 35 ml at a pressure P_i = 101 kPa. The predicted transient mass flux G_{in}, temperature T_s of the heat sink, and instantaneous heat absorbed by the fluid ($q^* = hA_s(T_s - T_f)$) are shown in Figure 7. During the pressure drop oscillation cycle, the channel experiences a period of time where mass flux is lower than the nominal value (shown as a horizontal dashed black line in Figure 7(a)) followed by a period of increased mass flux. During the low-mass-flux portion of the cycle, the temperature of the fluid within the channel is high and the instantaneous heat absorbed by the liquid is less than the total heat input (shown as a horizontal dashed black line in Figure 7(c)). This results in a steady increase in heat sink temperature until the upstream pressure recovers and the heat sink is supplied again with subcooled liquid at a higher mass flux, resulting in an increase in instantaneous heat absorbed by the fluid above the total heat input and a rapid reduction in heat sink temperature. From these dynamic predictions, the frequency of the oscillation and the peak-to-peak temperature amplitude can also be extracted. In this case, the frequency of the oscillation is f = 0.33 Hz and the peak-to-peak temperature amplitude is 2.2 C.

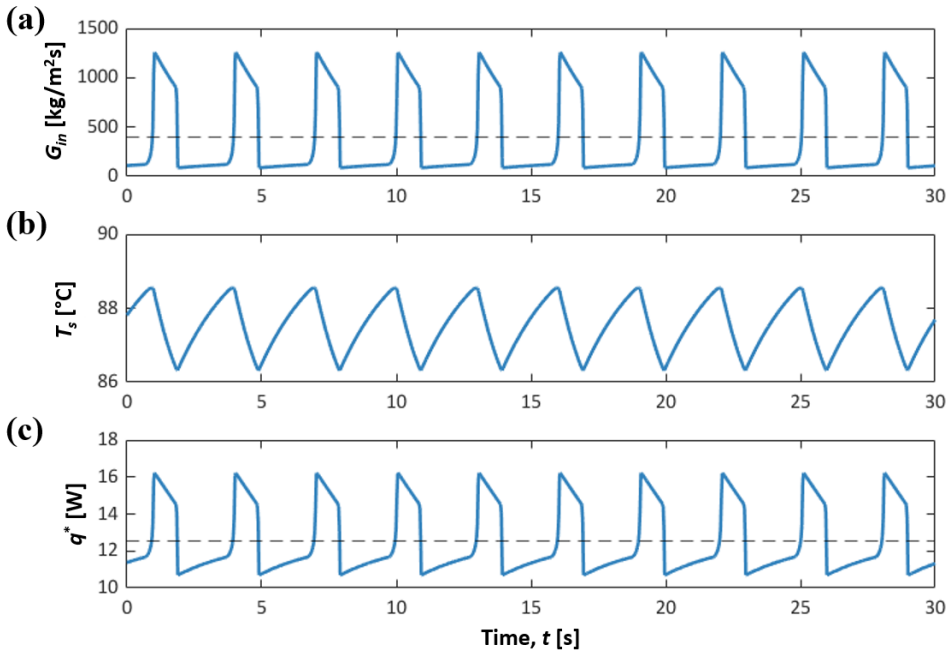

Figure 7. Dynamic model predictions of (a) channel mass flux G_{in}, (b) heat sink temperature T_s, and (c) instantaneous heat absorbed by the fluid q^* during pressure drop oscillations in a w_c = 0.75 mm channel with nominal mass flux of G_{buf} = 400 kg/m^{2}s and heat flux of q" = 24 W/cm^2.

3.3 Experimental Comparison

In this section, experiments performed as part of a previous study [24] are compared with model predictions. The experiments were performed using the same experimental facility described in Section 2 with one key difference: the heater used in these experiments was a large copper block with overall dimensions of 2 cm × 2 cm × 4 cm with cartridge heaters. The experimental data set for comparison considers heat sink geometries with nominal channel widths w_c = 0.5 mm, 0.75 mm, and 1 mm. The mean measured channel geometries are listed in Table 2. Due to the larger surface area of the copper heater block, heat losses are more significant, and the measured electrical power input is corrected by an experimentally calibrated heat loss factor [23] for heat flux calculation ($q" = (P_{elec} - Q_{loss})/A_s$). Each experiment in this data set is performed with power increments from zero up to critical heat flux.

Table 2. Measured heat sink channel geometry.

Number of Channels, N	Mean Channel Width, w_c [mm]	Mean Channel Height, h_c [mm]
19	0.55	0.47

12	0.85	0.83
10	1.04	0.99

While the model is derived for flow through a single channel, it is used here to compare against experimental data for an array of parallel channels by assuming that each channel exhibits the same behavior and pressure demand curve. Model inputs that are constant across all experiment cases are listed in Table 3.

Table 3. Summary of model inputs for comparison with experiments.

Parameter	**Value**
Channel length, L_c [mm]	20
Initial compressible volume (CV), V_i [ml]	35
Initial pressure of CV, P_i [kPa]	101
Mass flux, G_{buf} [kg/m^{2}s]	400
Inlet temperature, T_{in} [°C]	41
Copper specific heat capacity, C_p [J/kgK]	376

Other model inputs, specifically the heat input, heat transfer coefficient, and the effective lumped thermal capacitance ($m_{eff}C_p$) of the heat sink, are different for each case. The total heat input q' is calculated using the heat-loss-corrected electrical power input.

$$q' = \frac{P_{elec} - Q_{loss}}{N * (2h_c + w_c)} \tag{4}$$

Heat transfer coefficients are calculated using the mean extrapolated surface temperature from the three thermocouples and a length-weighted average fluid reference temperature assuming that the fluid is at the saturation temperature evaluated at atmospheric pressure wherever the local vapor quality $x > 0$.

$$h = \frac{q"}{T_s - T_{ref}} \tag{5}$$

For the range of oscillation frequencies observed in the experiments (0.2 – 0.5 Hz), the thermal penetration depth into a semi-infinite solid ($\delta_{p,\omega} = 4\sqrt{\alpha/(2\pi f)}$) is between 2 – 4 cm. This is significantly less than the total depth of the heat sink when attached to a large copper block, so that only a portion of the mass will fluctuate in temperature in response to the oscillations occurring at the surface.

Furthermore, because the model assumes a lumped thermal mass, we must estimate an effective lumped thermal mass representative of the actual thermal mass in the system which does respond to the transient oscillations at the surface.

To estimate an effective thermal mass, the penetration depth due to a step change in surface temperature is calculated ($\delta_p = 2\sqrt{\alpha t}$) using a time equal to half the oscillation period. The temperature profile within the semi-infinite solid medium at a particular time is analytically represented by the complimentary error function

$$\frac{T(x,t) - T_i}{T_s - T_i} = \text{erfc}\left(\frac{x}{\delta_p}\right) \tag{6}$$

In this case, the initial temperature T_i is taken as the time-averaged temperature T_{mean} and T_s is the instantaneous peak in channel surface temperature. The total change in internal energy of the solid at time $t = \lambda/2$ can be approximated by integrating $T(x,t) - T_{mean}$ from the surface to the penetration depth.

$$\Delta Q = \rho_w A_f C_p (T_s - T_{mean}) \int_0^{\delta_p} \text{erfc}\left(\frac{x}{\delta_p}\right) dx \tag{7}$$

The change in internal energy of a lumped mass with effective depth d_{eff} experiencing the same change in temperature from T_{mean} to T_s is calculated as

$$\Delta Q = \rho_w A_f d_{eff} C_p (T_s - T_{mean}) \tag{8}$$

By equating Equations (7) and (8), the depth of the effective lumped thermal mass can be calculated.

$$d_{eff} = \int_0^{\delta_p} \text{erfc}\left(\frac{x}{\delta_p}\right) dx \tag{9}$$

The effective lumped thermal mass $m_{eff} = \rho_w A_f d_{eff}$ can then be used in the model to represent the thermal mass within the experiment, where A_f is the footprint area of a single channel ($4\ cm^2/N$). Since δ_p depends on the period of the PDO, an initial guess must be made. In this case, the model is first solved using a lumped thermal mass with depth of 10 mm. The resulting PDO period then is used to calculate a new δ_p and m_{eff} with one iteration, which are then used in the final model prediction.

The steady-state heat fluxes at which pressure drop oscillations were observed in the experiments are compared against model predictions for the same geometric and flow conditions in Table 4. For each heat sink geometry and heat flux, the experimentally measured frequency of oscillation and temperature peak-to-peak amplitude is shown on the left side of the table. The frequency is calculated using a fast Fourier transform (FFT) analysis of both the inlet pressure signal and thermocouple signals. On the right side of the table, the model-predicted oscillation frequency and peak-to-peak temperature amplitudes are

shown on the corresponding row. Additionally, the calculated effective thermal capacitance is reported in the final column.

Table 4. Comparison of model predictions and experiment results at a mass flux of G = 400 kg/m^{2}s and inlet subcooling of T_{sub} = 20 °C.

		EXPERIMENTS		**MODEL**		
Channel width, w_c [mm]	Heat Flux, q" [W/cm^2]	Frequency, f [Hz]	$T_{s,max} - T_{s,min}$ [°C]	Frequency, f [Hz]	$T_{s,max} - T_{s,min}$ [°C]	Thermal Capacitance, $m_{eff}C_p$ [J/K]
0.5	12	0.27	1.1	0.33	0.7	1.19
	17	0.28	1.4	0.16	1.2	1.92
	21	0.22	1.8	0.07	1.9	2.43
0.75	20	0.50	1.3	0.53	1.2	1.20
	24	0.40	1.7	0.38	1.5	1.44
	28	0.24	2.3	0.28	1.7	1.72
1	19	0.44	1.4	0.45	1.1	1.58
	21	0.30	2.8	0.36	1.2	1.75

For a given heat sink channel width, as heat flux increases the experimentally measured PDO frequency decreases and the temperature amplitude increases. There is one exception to this trend in the experiments at the lowest heat flux of q" = 12 W/cm^2 in the w_c = 0.5 mm heat sink. In this case, the heat flux is near the lower end of heat fluxes where PDOs are observed to occur. In this lower range, it was observed in previous experimental work that oscillations are often unsteady and do not exhibit the regular periodic fluctuation observed during PDO [24]. Furthermore, the trend of decreasing oscillation frequency and increasing temperature amplitude with increasing heat flux is predicted by the model. As shown in the final column of Table 4, the estimated effective thermal capacitance increases with increasing heat flux due to the decreasing oscillation frequency and resulting increase in penetration depth.

In terms of absolute values, good agreement is observed between the experimental and predicted PDO frequency values for both the w_c = 0.75 mm and 1 mm heat sinks. For the smallest w_c = 0.5 mm heat sink, the model predicts notably lower frequencies than observed in the experiments for the highest heat flux. Because the thermal penetration depth increases with decreasing oscillation frequency, this discrepancy is likely due to error associated with the simplification of assuming an effective lumped thermal mass, for which a direct validation across all conditions is not expected. Nevertheless, even under

this lumped mass simplification, the comparison demonstrates the model's capability to accurately predict the trends in the severity of pressure oscillations and impact on thermal response at various heat fluxes.

4 Effect of Thermal Capacitance

The model described above can be exercised to better understand the effect of thermal capacitance on the response of a heat sink to pressure drop oscillations. In this section, the model is used to predict pressure drop oscillation dynamics and thermal response of a heat sink with two different amounts of thermal capacitance. The first per-channel thermal capacitance of $m_{eff}C_p$ = 1.08 J/K corresponds to a lumped thermal mass of copper with the same footprint area as the heat sinks used in the experiments (2 cm × 2 cm) and a height of 10 mm. The second thermal capacitance is chosen to be $m_{eff}C_p$ = 0.35 J/K, a reduction of 68%, which corresponds to a much shorter heat sink height of 3.5 mm for the same footprint. Other inputs to the model for this demonstration are taken from the case in Table 4 corresponding to the nominal w_c = 0.75 mm and q'' = 24 W/cm^2 and are listed in Table 5 below.

Table 5. Model inputs for demonstrating effect of thermal capacitance.

Parameter	**Value**
Channel length, L_c [mm]	20
Channel width, w_c [mm]	0.85
Channel height, h_c [mm]	0.83
Initial compressible volume (CV), V_i [ml]	35
Initial pressure of CV, P_i [kPa]	101
Mass flux, G_{buf} [kg/m^{2}s]	400
Heat input, q' [W/m]	600
Inlet temperature, T_{in} [°C]	41
Heat transfer coefficient, h [W/m^{2}K]	7400
Copper specific heat capacity, C_p [J/kgK]	376

The predicted transient channel mass flux and thermal response for the inputs listed in Table 5 and thermal capacitances of 1.08 J/K and 0.35 J/K are shown in Figure 8. Pressure drop oscillations are predicted to occur in both cases. During the portion of the limit cycles at a low mass flux, the quality of the fluid is high and therefore is at a higher average temperature. The heat sink temperature gradually

increases during this time until the upstream pressure recovers, and a high mass flux is again supplied to the channel and T_s decreases. This limit cycle continues in a time-periodic manner. Comparing the two thermal capacitances, a slight increase in the amplitude of mass flux oscillations G_{in} and a reduction in oscillation frequency is observed when the thermal capacitance is reduced from 1.08 J/K to 0.35 J/K. This indicates that the thermal capacitance influences the dynamics of the pressure drop oscillation, and not only the temperature response, due to the coupling between the flow and heat transfer dynamics in the system. Specifically, this coupling is due to sensitivity of the quality of the flow, and thereby the channel pressure drop, to the instantaneous heat absorbed by the fluid $q^* = hA_s(T_s - T_f)$ which determines the instantaneous temperature of the heat sink. In terms of thermal response, reducing the thermal capacitance by 68% has a significant impact on the peak-to-peak temperature amplitude, increasing 240% from 2.1 °C to 7.2 °C. While the peak temperatures are predicted to increase by approximately 1.9 °C, the minimum temperature is predicted to decrease by 3.1 °C. To experimentally demonstrate this behavior, physical experiments are performed under the same conditions.

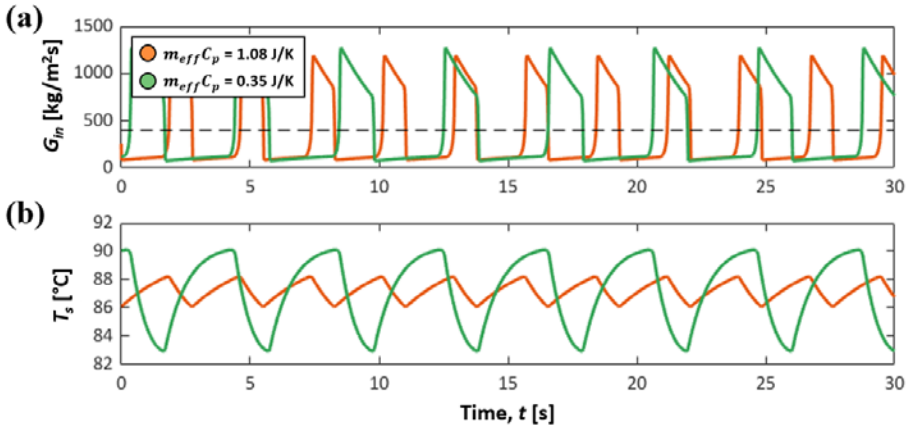

Figure 8. Dynamic model predictions of (a) channel mass flux G_{in} and (b) heat sink temperature T_s during pressure drop oscillations in heat sinks with thermal capacitances of $m_{eff}C_p$ = 1.08 J/K (orange) and 0.35 J/K (green) using the model inputs listed in Table 5.

Two experiments are performed at the nominal conditions listed in Table 5 and additional heat fluxes q'' = 16, 20, and 28 W/cm^2. The first experiment is performed in the w_c= 0.75 mm heat sink with an overall copper block height of 10 mm combined with the ceramic heater. For the second experiment, the copper heat sink block is machined down to an overall height of 3.5 mm to yield a lower thermal

capacitance. This is the minimum height to which the heat sink can be reduced while retaining the same placement of thermocouple taps for consistency. Photographs of the heat sink before and after reducing the height are shown in Figure 9.

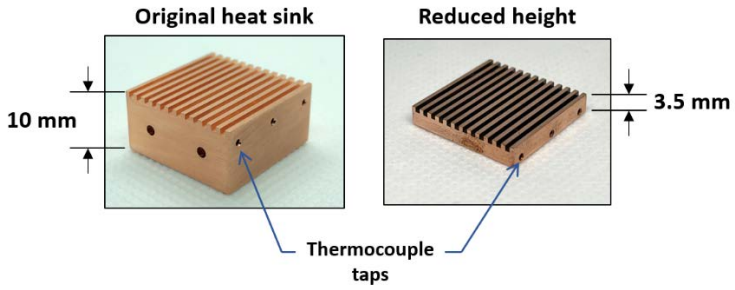

Figure 9. Photographs of the w_c = 0.75 mm heat sink before and after reducing the copper block height from 10 mm to 3.5 mm.

In Figure 10, the transient 14 Hz signal recorded from the middle thermocouple embedded in the heat sink is shown at each heat flux for the large thermal capacitance (orange) and small thermal capacitance (green). The amplitude and frequency of PDO oscillations at each heat flux are summarized in Table 6. Amplitudes are represented as the difference between the 95th percentile $T_{2,95}$ and 5th percentile $T_{2,5}$ of temperatures plotted in Figure 10. Frequencies are calculated as the average time between the highest temperature peaks. The lowest heat flux, shown in Figure 10(a), demonstrates a case at the lower range of heat fluxes where PDOs are observed to occur and oscillations are present, but are often unsteady or irregular. Even in this case, the effect of decreasing the heat sink mass is apparent, as the amplitude of temperature oscillations increases significantly. This is also true for the higher heat fluxes shown in Figure 10 (b) and (c). In both cases, the mean temperature and peak-to-peak temperature oscillation amplitude observed in the lower-thermal-capacitance heat sink are significantly higher than those observed in identical channels with the larger thermal capacitance. The oscillation frequency is also impacted, decreasing with a reduction in thermal capacitance, though this effect is less apparent. At the highest heat flux of q'' = 28 W/cm^2, steady pressure drop oscillations observed in the larger-thermal-capacitance heat sink follow the same trends of decreasing frequency and increasing temperature amplitude with increasing heat flux. However, after reducing the mass of the heat sink, CHF is reached at this heat flux. In the transient temperature signal, a temperature excursion occurs at one of the peaks in the temperature oscillation cycle, clearly indicating that the PDO instability was the trigger of CHF.

Further evidence is found from comparing the CHF in the low-thermal-capacitance heat sink with the CHF from our previous work under identical conditions but much larger thermal capacitance [24], where we find a 21% decrease in the low-thermal-capacitance CHF. This indicates that, with sufficient thermal capacitance, the fluid can recover after low mass flux, high-quality periods during the PDO cycle and prevent early occurrence of CHF. However, if there is insufficient thermal capacitance, the fluid is unable to recover, and early onset of CHF may occur due to pressure drop oscillations.

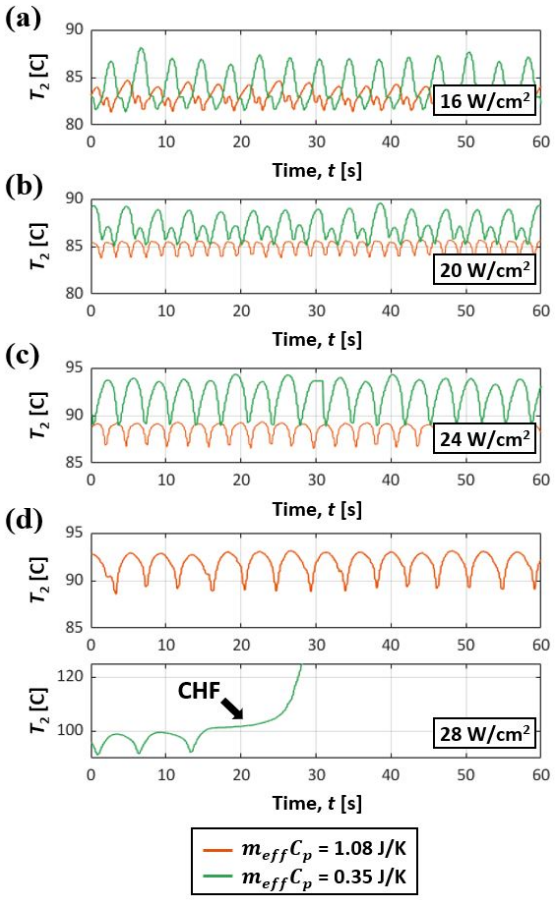

Figure 10. Transient signals from the middle thermocouple in the large-mass (orange) and low-mass (green) heat sinks at heat fluxes of (a) q" = 16 W/cm^2, (b) q" = 20 W/cm^2, (c) q" = 24 W/cm^2, and (d) q" = 28 W/cm^2.

Table 6. Amplitude and frequency of oscillations at heat fluxes of q" = 16, 20, 24, and 28 W/cm^2 for the large-mass and low-mass heat sinks.

	$m_{eff}C_p$ = 1.08 J/K	$m_{eff}C_p$ = 0.35 J/K

Heat Flux, q"	$T_{2,95} - T_{2,5}$	Frequency, f	$T_{2,95} - T_{2,5}$	Frequency, f
16 W/cm^2	2.7 °C	0.25 Hz	5.4 °C	0.25 Hz
20 W/cm^2	1.6 °C	0.50 Hz	3.6 °C	0.24 Hz
24 W/cm^2	2.4 °C	0.37 Hz	4.8 °C	0.29 Hz
28 W/cm^2	3.7 °C	0.24 Hz	-	-

5 Conclusions

The role of heat sink thermal capacitance on microchannel heat sink performance in the presence of the pressure drop oscillation instability is explored through dynamic modeling and experiments. The model, which considers dynamic two-phase flow interactions between a heated microchannel with thermal mass and an upstream compressible volume, is first compared with a large data set of experiments performed in a previous study [24]. This comparison shows good agreement of trends in pressure drop oscillation frequency and peak-to-peak temperature amplitudes for a range of heat fluxes. These model predictions then inspired a case study to demonstrate that a heat sink with large versus small thermal capacitance, under otherwise identical conditions, may have dramatically different system dynamics due to the close coupling between the flow and heat transfer. Specifically, the model indicated that a reduction in heat sink thermal capacitance would result in lower-frequency pressure drop oscillations having more severe peak-to-peak temperature swings. To confirm this behavior, targeted experiments are performed in two heat sinks of different thermal capacitances. The observations from these experiments clearly confirm the model-predicted behavior. Furthermore, the experiments reveal that, if thermal capacitance is low, pressure drop oscillations may result in an early onset of critical heat flux. Conversely, if thermal capacitance is sufficiently high, the system is able to recover during the portion of the limit cycle when the channel has a low mass flux, preventing temperature excursion and CHF during pressure drop oscillation instability.

Appendix

The header losses ΔP_i and ΔP_o used in the model need to be calibrated to the pressure losses in the experimental test section. These losses include flow through bends in the plenums and contraction into and expansion out of the channels.

$$\Delta P_i = \Delta P_{cont} + \Delta P_{90} \quad \text{(A1)}$$

$$\Delta P_o = \Delta P_{exp} + \Delta P_{90} \quad \text{(A2)}$$

Contraction and expansion pressure losses are calculated using correlations developed in Ref. [34] specifically for parallel microchannel heat sinks.

$$\Delta P_{cont} = \left[1 - \left(\frac{N * A_c}{A_{header}}\right)^2 + K_c\right]\left(\frac{G_{in}^2}{2\rho_f}\right) \tag{A3}$$

$$K_c = 0.0088(h_c/w_c)^2 - 0.1785(h_c/w_c) + 1.6027 \tag{A4}$$

$$\Delta P_{exp} = -2\beta\left(\frac{N * A_c}{A_{header}}\right)\left[1 - \frac{N * A_c}{A_{header}}\right]\left(\frac{G_{in}^2}{2\rho_f}\right) \tag{A5}$$

In Equations (A3) and (A5), A_{header} is the cross-section area of the inlet and outlet headers and the flow profile factor β = 1.33 according to Ref. [34]. Pressure loss in the plenums ΔP_{90} is calculated according to Ref. [35].

$$\Delta P_{90} = \left(\frac{G_{in}^2}{2\rho_f}\right)\left[\left(\frac{A_{header}}{A_{plenum}}\right)^2 * 2 * K_{90}\right] \tag{A6}$$

The coefficient $K_{90} = 2$ is obtained by calibration to experimental pressure drop data and area A_{plenum} is the cross-sectional area of the inlet and outlet plenums.

Acknowledgements

This material is based upon work supported by Ford Motor Company through the Ford – Purdue University Alliance program. Special thanks to Dr. Edward Jih at Ford Research & Advanced Engineering (R&AE) for technical discussions related to this work.

References

[1] A. Bar-Cohen, M. Arik, and M. Ohadi, "Direct Liquid Cooling of High Flux Micro and Nano Electronic Components," *Proc. IEEE*, vol. 94, no. 8, pp. 1549–1570, 2006, doi: 10.1109/JPROC.2006.879791.

[2] K. P. Bloschock and A. Bar-Cohen, "Advanced thermal management technologies for defense electronics," in *Defense Transformation and Net-Centric Systems 2012*, 2012, vol. 8405, p. 84050I. doi: 10.1117/12.924349.

[3] A. Bar-Cohen, J. J. Maurer, and J. G. Felbinger, "DARPA's Intra/Interchip Enhanced Cooling (ICECool) Program," in *Proc. CS MANTECH Conference*, New Orleans, LA, USA, 2013, pp. 171–174.

[4] A. Bar-Cohen, J. J. Maurer, and D. H. Altman, "Embedded Cooling for Wide Bandgap Power Amplifiers: A Review," *J. Electron. Packag.*, vol. 141, no. 4, 2019, doi: 10.1115/1.4043404.

[5] K. P. Drummond *et al.*, "Characterization of hierarchical manifold microchannel heat sink arrays under simultaneous background and hotspot heating conditions," *Int. J. Heat Mass Transf.*, vol. 126, pp. 1289–1301, 2018, doi: 10.1016/j.ijheatmasstransfer.2018.05.127.

[6] A. Bar-Cohen *et al.*, "The ICECool Fundamentals Effort on Evaporative Cooling of Microelectronics," *IEEE Trans. Compon. Packag. Manuf. Technol.*, vol. 11, no. 10, pp. 1546–1564, 2021, doi: 10.1109/TCPMT.2021.3111114.

[7] R. K. Mandel, D. G. Bae, and M. M. Ohadi, "Embedded Two-Phase Cooling of High Flux Electronics Via Press-Fit and Bonded FEEDS Coolers," *J. Electron. Packag.*, vol. 140, no. 3, 2018, doi: 10.1115/1.4039264.

[8] Y. K. Prajapati and P. Bhandari, "Flow boiling instabilities in microchannels and their promising solutions – A review," *Exp. Therm. Fluid Sci.*, vol. 88, pp. 576–593, 2017, doi: 10.1016/j.expthermflusci.2017.07.014.

[9] S. Kakac and B. Bon, "A Review of two-phase flow dynamic instabilities in tube boiling systems," *Int. J. Heat Mass Transf.*, vol. 51, no. 3, pp. 399–433, 2008, doi: 10.1016/j.ijheatmasstransfer.2007.09.026.

[10] J. A. Boure, A. E. Bergles, and L. S. Tong, "Review of two-phase flow instability," *Nucl. Eng. Des.*, vol. 25, no. 2, pp. 165–192, 1973, doi: 10.1016/0029-5493(73)90043-5.

[11] T. A. Kingston, J. A. Weibel, and S. V. Garimella, "Ledinegg instability-induced temperature excursion between thermally isolated, heated parallel microchannels," *Int. J. Heat Mass Transf.*, vol. 132, pp. 550–556, 2019, doi: 10.1016/j.ijheatmasstransfer.2018.12.017.

[12] A. Miglani, J. A. Weibel, and S. V. Garimella, "Measurement of flow maldistribution induced by the Ledinegg instability during boiling in thermally isolated parallel microchannels," *Int. J. Multiph. Flow*, vol. 139, p. 103644, 2021, doi: 10.1016/j.ijmultiphaseflow.2021.103644.

[13] A. Miglani, J. A. Weibel, and S. V. Garimella, "An experimental investigation of the effect of thermal coupling between parallel microchannels undergoing boiling on the Ledinegg instability-induced flow maldistribution," *Int. J. Multiph. Flow*, vol. 139, p. 103536, 2021, doi: 10.1016/j.ijmultiphaseflow.2020.103536.

[14] T. Van Oevelen, J. A. Weibel, and S. V. Garimella, "Predicting two-phase flow distribution and stability in systems with many parallel heated channels," *Int. J. Heat Mass Transf.*, vol. 107, pp. 557–571, 2017, doi: 10.1016/j.ijheatmasstransfer.2016.11.050.

[15] S. G. Kandlikar, *Handbook of Phase Change : Boiling and Condensation*, 1st ed. Boca Raton, FL, USA: CRC Press, 1999. doi: 10.1201/9780203752654.

[16] G. P. Celata, S. K. Saha, G. Zummo, and D. Dossevi, "Heat transfer characteristics of flow boiling in a single horizontal microchannel," *Int. J. Therm. Sci.*, vol. 49, no. 7, pp. 1086–1094, 2010, doi: 10.1016/j.ijthermalsci.2010.01.019.

[17] Y. Wang and K. Sefiane, “Effects of heat flux, vapour quality, channel hydraulic diameter on flow boiling heat transfer in variable aspect ratio micro-channels using transparent heating,” *Int. J. Heat Mass Transf.*, vol. 55, no. 9, pp. 2235–2243, 2012, doi: 10.1016/j.ijheatmasstransfer.2012.01.044.
[18] Y. Wang, K. Sefiane, Z. Wang, and S. Harmand, “Analysis of two-phase pressure drop fluctuations during micro-channel flow boiling,” *Int. J. Heat Mass Transf.*, vol. 70, pp. 353–362, 2014, doi: 10.1016/j.ijheatmasstransfer.2013.11.012.
[19] G. Wang, P. Cheng, and A. E. Bergles, “Effects of inlet/outlet configurations on flow boiling instability in parallel microchannels,” *Int. J. Heat Mass Transf.*, vol. 51, no. 9, pp. 2267–2281, 2008, doi: 10.1016/j.ijheatmasstransfer.2007.08.027.
[20] S. Szczukiewicz, N. Borhani, and J. R. Thome, “Two-phase heat transfer and high-speed visualization of refrigerant flows in 100 × 100 μm2 silicon multi-microchannels,” *Int. J. Refrig.*, vol. 36, no. 2, pp. 402–413, 2013, doi: 10.1016/j.ijrefrig.2012.11.014.
[21] S. G. Kandlikar, W. K. Kuan, D. A. Willistein, and J. Borrelli, “Stabilization of Flow Boiling in Microchannels Using Pressure Drop Elements and Fabricated Nucleation Sites,” *J. Heat Transf.*, vol. 128, no. 4, pp. 389–396, 2005, doi: 10.1115/1.2165208.
[22] Y. Li, G. Xia, Y. Jia, Y. Cheng, and J. Wang, “Experimental investigation of flow boiling performance in microchannels with and without triangular cavities – A comparative study,” *Int. J. Heat Mass Transf.*, vol. 108, pp. 1511–1526, 2017, doi: 10.1016/j.ijheatmasstransfer.2017.01.011.
[23] M. D. Clark, J. A. Weibel, and S. V. Garimella, “Impact of Pressure Drop Oscillations on Surface Temperature and Critical Heat Flux during Flow Boiling in a Microchannel,” *IEEE Trans. Compon. Packag. Manuf. Technol.*, pp. 1634–1644, 2021, doi: 10.1109/TCPMT.2021.3094767.
[24] M. D. Clark, J. A. Weibel, and S. V. Garimella, “Impact of Pressure Drop Oscillations and Parallel Channel Instabilities on Microchannel Flow Boiling and Critical Heat Flux,” *IJMF Rev.*, 2022.
[25] T. A. Kingston, J. A. Weibel, and S. V. Garimella, “High-frequency thermal-fluidic characterization of dynamic microchannel flow boiling instabilities: Part 2 – Impact of operating conditions on instability type and severity,” *Int. J. Multiph. Flow*, 2018, doi: 10.1016/j.ijmultiphaseflow.2018.05.001.
[26] M. E. Rahman and J. A. Weibel, “Mapping the amplitude and frequency of pressure drop oscillations via a transient numerical model to assess their severity during microchannel flow boiling,” *Int. J. Heat Mass Transf.*, vol. 194, p. 123065, 2022, doi: 10.1016/j.ijheatmasstransfer.2022.123065.
[27] M. M. Padki, H. T. Liu, and S. Kakac, “Two-phase flow pressure-drop type and thermal oscillations,” *Int. J. Heat Fluid Flow*, vol. 12, no. 3, pp. 240–248, 1991, doi: 10.1016/0142-727X(91)90058-4.
[28] P. R. Mawasha and R. J. Gross, “Periodic oscillations in a horizontal single boiling channel with thermal wall capacity,” *Int. J. Heat Fluid Flow*, vol. 22, no. 6, pp. 643–649, 2001, doi: 10.1016/S0142-727X(01)00115-1.
[29] T. Zhang *et al.*, “Analysis and active control of pressure-drop flow instabilities in boiling microchannel systems,” *Int. J. Heat Mass Transf.*, vol. 53, no. 11, pp. 2347–2360, 2010, doi: 10.1016/j.ijheatmasstransfer.2010.02.005.
[30] E. Manavela Chiapero, M. Fernandino, and C. A. Dorao, “On the influence of heat flux updating during pressure drop oscillations – A numerical analysis,” *Int. J. Heat Mass Transf.*, vol. 63, pp. 31–40, 2013, doi: 10.1016/j.ijheatmasstransfer.2013.03.047.
[31] M. E. Rahman and J. A. Weibel, “Influence of convective heat transfer and wall thermal capacity on dynamic interactions between wall temperature and pressure drop oscillations during microchannel flow boiling,” *Int. J. Heat Mass Transf.* (In Review), 2023.
[32] L. E. O’Neill and I. Mudawar, “Review of two-phase flow instabilities in macro- and micro-channel systems,” *Int. J. Heat Mass Transf.*, vol. 157, p. 119738, 2020, doi: 10.1016/j.ijheatmasstransfer.2020.119738.

[33] *3M Novec Engineered Fluid HFE-7100 for Heat Transfer*. St. Paul, MN, USA: 3M, 2002.
[34] D. Liu and S. V. Garimella, “Investigation of Liquid Flow in Microchannels,” *J. Thermophys. Heat Transf.*, vol. 18, no. 1, pp. 65–72, 2004, doi: 10.2514/1.9124.
[35] S. Kandlikar, S. Garimella, D. Li, S. Colin, and M. R. King, *Heat Transfer and Fluid Flow in Minichannels and Microchannels*, 1st ed. San Diego, CA: Elsevier, 2005.
[36] *MATLAB version 9.10.0.1710957 (R2021a) Update 4*. Natick, Massachusetts: The Mathworks, Inc., 2021.